Research Square

Preprints are preliminary reports that have not undergone peer review.
They should not be considered conclusive, used to inform clinical practice,
or referenced by the media as validated information.

Effects of Eccentricity on Nonlinear Dynamic Behaviors of a Rotor Subjected to Clearance Fit between Bearing Outer Ring and Housing

Haifei Wang

hfwang@nuaa.edu.cn

Nanjing University of Aeronautics and Astronautics

Kelong Guo

Nanjing University of Aeronautics and Astronautics

Xunkai Liang

Nanjing University of Aeronautics and Astronautics

Tian Zhou

Nanjing University of Aeronautics and Astronautics

Chao Dong

AECC Shenyang Engine Research Institute

Zhenhuan Tang

AECC Hunan Aviation Powerplant Research Institute

Kian Meng Lim

National University of Singapore

Research Article

Keywords: Rotor system, Radial clearance, Nonlinear vibration, Eccentricity, Bearing outer ring, Self-excited oscillation

Posted Date: October 8th, 2026

DOI: https://doi.org/10.21203/rs.3.rs-10960244/v1

License: This work is licensed under a Creative Commons Attribution 4.0 International License.
Read Full License

Additional Declarations: No competing interests reported.

Effects of Eccentricity on Nonlinear Dynamic Behaviors of a Rotor Subjected to Clearance Fit between Bearing Outer Ring and Housing

Haifei Wang[1,2*], Kelong Guo[1], Xunkai Liang[1], Tian Zhou[3], Chao Dong[4,5], Zhenhuan Tang[6], Kian Meng Lim[7]

[1*] College of General Aviation and Flight, Nanjing University of Aeronautics and Astronautics, No. 29 Binhe East Road, Liyang, 213300, Jiangsu, China .

[2] State Key Laboratory of Mechanical Transmission for Advanced Equipment, Chongqing University, Chongqing, 400044, China .

[3] Department of Public Experimental Teaching, Nanjing University of Aeronautics and Astronautics, No. 29 Binhe East Road, Liyang, 213300, Jiangsu, China .

[4] , AECC Shenyang Engine Research Institute, Shenyang, 110015, Liaoning, China .

[5] , National Key Laboratory of Advanced Marine Engine Technology, Shenyang, 110015, Liaoning, China .

[6] , AECC Hunan Aviation Powerplant Research Institute, Zhuzhou, 412002, Hunan, China .

[7] College of Design and Engineering, National University of Singapore, 9 Engineering Drive 1, Block EA 07-08, Singapore, 117575, Singapore .

*Corresponding author(s). E-mail(s): hfwang@nuaa.edu.cn;
Contributing authors: guokelong@nuaa.edu.cn; 172744471@qq.com; 1696391929@qq.com; 976707302@qq.com; 18732086@qq.com; limkm@nus.edu.sg;

Abstract

This paper presents a systematic numerical study on the nonlinear dynamic behavior of a flexible rotor system with radial clearance between the bearing

outer ring and the housing, with particular emphasis on the effect of dimensionless eccentricity. A four-degree-of-freedom dynamic model is established using Lagrange's principle, in which the elastic collisions between the bearing outer ring and the housing are characterized by a restitution-coefficient-based impact model. The equations of motion are solved numerically by the fourth-order Runge–Kutta method, with an event-driven procedure to accurately detect the collision and non-collision states. The proposed model is first validated against the benchmark numerical results of Ishida et al[1]. under low-eccentricity conditions, where good agreement is achieved in terms of orbital topologies, time-domain waveforms, and frequency spectra. Subsequently, the validated model is employed to investigate the influence of dimensionless eccentricity on the system responses under three typical levels: low ($\boldsymbol{e = 0.1}$), moderate ($\boldsymbol{e = 0.5}$), and high ($\boldsymbol{e = 1.0}$). The numerical results reveal that the eccentricity plays a modulating role in the occurrence and intensity of nonlinear phenomena. At low eccentricity, the system exhibits abundant nonlinear resonances, including subharmonic, superharmonic, combination resonances, and self-excited vibrations. As the eccentricity increases to a moderate level, the superharmonic and subharmonic resonances become more pronounced. At high eccentricity, however, the nonlinear responses tend to be dominated by quasi-periodic motions, and the types of combination resonances are significantly reduced. These findings provide theoretical insights into the vibration diagnosis and fault prevention of rotor systems with clearance fit, particularly under varying operating conditions.

Keywords: Rotor system, Radial clearance, Nonlinear vibration, Eccentricity, Bearing outer ring, Self-excited oscillation

1 Introduction

Rotating machinery such as aero-engines, gas turbines, and high-speed spindles widely employs squeeze film dampers to suppress vibrations and ensure operational stability. However, during long-term service, seal aging or impact-induced damage may lead to lubricant leakage, consequently generating a radial clearance between the bearing outer ring and the housing. This clearance fit alters the support characteristics of the rotor system and may induce repeated impact and friction between the bearing outer ring and the housing, giving rise to strong nonlinear vibrations that severely affect the reliability and service life of the entire system [2, 3].

Clearances in rotor-bearing systems can be broadly classified into two categories: clearance between the rotor and the stator (e.g., seals and blade tips), and clearance between stationary components (e.g., between a bearing outer ring and its pedestal). In the first category, rotor-stator rub-impact has been extensively studied. Chu and Zhang [4] investigated bifurcation and chaos in a rub-impact Jeffcott rotor system, revealing period-doubling, quasi-periodic, and chaotic motions with increasing speed. Hou et al. [5] further analyzed the bifurcation and stability of a nonlinear rotor under constant excitation and rub-impact, showing that increased rotor damping can effectively suppress bifurcation. Ehehalt et al. [6] examined multiple motion patterns arising from rotor-stator contact under dry friction, identifying synchronous

forward whirl, backward whirl, subharmonic and superharmonic responses, and chaotic motions. More recently, Li et al. [7] investigated the nonlinear dynamics of deterministic rotor systems with rub-impact faults under maneuvering flight, revealing the effects of geometrical nonlinearity on rub-impact responses.

In the second category, clearances between stationary components are of particular practical significance. Ehrich [8] reported the occurrence of high-order subharmonic responses in high-speed rotors with bearing clearance. Childs [9] analyzed fractional-frequency rotor motions due to nonsymmetric clearance effects. Choi and Noah [10] and Kim and Noah [11] systematically analyzed subharmonic and super-subharmonic resonances caused by piecewise linear stiffness characteristics. Tiwari et al. [12, 13] investigated the effect of radial internal clearance of ball bearings on the dynamics of both balanced and unbalanced horizontal rotors, identifying super-harmonic, subharmonic, and chaotic behavior. Harsha [14] further examined the nonlinear dynamic response of balanced rotors supported by rolling element bearings due to radial internal clearance effects.

Among the various types of clearance fit, the radial clearance between the bearing outer ring and the housing is of particular practical significance. In high-speed rotating machines, temperature variations and assembly pre-stressing inevitably lead to clearance fit between the bearing outer ring and the housing. Chen and Qu [2] established a rotor-rolling bearing dynamic model with bearing fit clearance fault and investigated the influence of fit clearance, rotor unbalance, and outer ring tightening torque on vibration responses. Their results demonstrated that fit clearance induces strong nonlinear vibrations and significantly reduces system reliability. Cao et al. [15] proposed a fully dynamic model of a rotor-bearing-pedestal system to investigate vibration characteristics and stability due to fit clearance, and verified the model through experiments. Xu et al. [16] proposed a three-dimensional clearance fit model between bearing rings and the bearing pedestal, and systematically analyzed the dynamic behaviors and contact characteristics of ball bearings under clearance fit effects. Liu et al. [3] investigated the vibration characteristics of a dual rotor-bearing outer ring-pedestal-casing system with clearance fit, revealing that clearance fit alters the support characteristics and dynamic behavior of the system. Wang et al. [17] experimentally studied the vibration of rotor systems caused by different assembly fits of the bearing outer ring in an aero-engine, finding that clearance fit induces subharmonic and super-subharmonic frequencies. Wu et al. [18] conducted a nonlinear dynamic analysis of rotor-bearing-pedestal systems with multiple fit clearances, highlighting the complex coupling effects of multiple clearances on system stability. Han et al. [19] performed a nonlinear dynamic analysis of flywheel rotor systems with multiple fit clearances, showing that the increase of fit clearance aggravates the vibration response level and shifts the resonance speed to low speed. Zhang et al. [20] studied the bearing fit effect on the vibration characteristics of spindle rotor-bearing systems, demonstrating that the influence of bearing fit on vibration is nonlinear and that rotor vibration is more sensitive to clearance fit of the outer ring than interference fit of the inner ring. Wang et al. [21] investigated the passive vibration reduction of a squeeze film damper for a rotor system with fit looseness between outer ring and housing, providing insights into the vibration suppression mechanisms under clearance conditions.

Lu et al. [22] analyzed the dynamic characteristics of a rotor-bearing system considering bearing clearance and hybrid eccentricity, revealing that the variation of rotor mixing eccentricity and bearing clearance leads to a complex coupling of nonlinear excitation forces.

The seminal work by Ishida et al. [1] provided comprehensive experimental and numerical investigations of nonlinear oscillations in a flexible rotor system with radial clearance between the bearing outer ring and the casing. Their study identified three major categories of nonlinear phenomena: (i) nonlinear resonances including subharmonic, super-subharmonic, and combination oscillations; (ii) self-excited oscillations of a forward whirling mode occurring in a wide range above the major critical speed; and (iii) entrainment phenomena from self-excited oscillation to nonlinear forced oscillation at resonance ranges. They further analyzed periodic solutions using the Harmonic Balance Method and explained the subharmonic resonance and its entrainment phenomenon theoretically by investigating the stability of periodic solutions. The theoretical foundations of rotor dynamics with clearance effects are also comprehensively summarized in the classic monograph by Yamamoto and Ishida [23].

The eccentricity of the rotor disk is a critical parameter that fundamentally affects the unbalance excitation and resulting nonlinear dynamic behavior of rotor systems. Zhao et al. [24] studied the nonlinear dynamic behavior of an elastic beam in large overall rotation with rotor eccentricity effect. Liu et al. [25] analyzed the nonlinear response of a rub-impact rotor-oil film bearing system and found that smaller eccentricity favors system stability at both low and high rotational speeds. Zhou et al. [26] observed that initial static eccentricity increases the amplitude of radial displacement and affects the trajectory's positional distribution. Zhang et al. [27] showed that geometric eccentricity can lead to anisotropic rotor-stator clearance and significantly affect system stability and dynamic bifurcation mechanisms. Despite these advances, the systematic and quantitative investigation of how dimensionless eccentricity modulates the nonlinear responses of a rotor system with clearance fit between the bearing outer ring and the housing remains limited.

To address this research gap, the present study establishes a four-degree-of-freedom dynamic model of a flexible rotor system with radial clearance between the bearing outer ring and the housing, based on Lagrange's principle. The elastic collisions between the bearing outer ring and the housing are characterized by a restitution-coefficient-based impact model. The equations of motion are solved numerically using the fourth-order Runge–Kutta method with an event-driven procedure to accurately detect collision and non-collision states. The proposed model is first validated against the benchmark numerical results of Ishida et al. [1]. Subsequently, the validated model is employed to systematically investigate the influence of dimensionless eccentricity on the system's nonlinear responses at three representative levels: low ($e = 0.1$), moderate ($e = 0.5$), and high ($e = 1.0$).

The remainder of this paper is organized as follows. Section 2 presents the physical model and mathematical formulation of the rotor system. Section 3 validates the proposed model against existing benchmark results. Section 4 systematically analyzes the effects of dimensionless eccentricity on the nonlinear responses. Finally, Section 5 concludes the paper with a summary of the main findings.

2 Physical Model and Mathematical Formulation

2.1 Physical Model

The present study investigates a flexible rotor system with radial clearance between the bearing outer ring and the housing, as illustrated in Fig. 1. The system consists of a thin disk rigidly mounted on a vertical elastic shaft, which is supported by two self-aligning double-row ball bearings at both ends. This type of bearing does not introduce nonlinearity to the restoring force of the shaft. The right-end bearing is designed with a radial clearance of approximately 0.1 mm between its outer ring and the housing, allowing the outer ring to move freely within the clearance in the radial direction.

The key geometrical parameters of the rotor system are listed in Table 1, where D and h denote the diameter and thickness of the disk, l is the length of the elastic shaft, d is the shaft diameter, and a and b are the distances from the disk to the left and right bearings, respectively.

Table 1: Geometrical parameters of the rotor system

Parameter	Value (mm)	Parameter	Value (mm)
Disk diameter D	480	Shaft length l	900
Disk thickness h	5.5	Shaft diameter d	16
Distance a	550	Distance b	350

The rotor system possesses two dominant vibration modes: the first mode corresponds to the lateral translational oscillation of the disk, which is dominant at lower frequencies, and the second mode corresponds to the tilting oscillation of the disk, which prevails at higher frequencies. To simplify the analysis, the nonlinear characteristics of the bearings and the mass of the shaft are neglected. The system is approximated by a four-degree-of-freedom model described by the coordinates (x_1, y_1) for the disk displacement and (x_2, y_2) for the displacement of the bearing outer ring, as shown in Fig. 2.

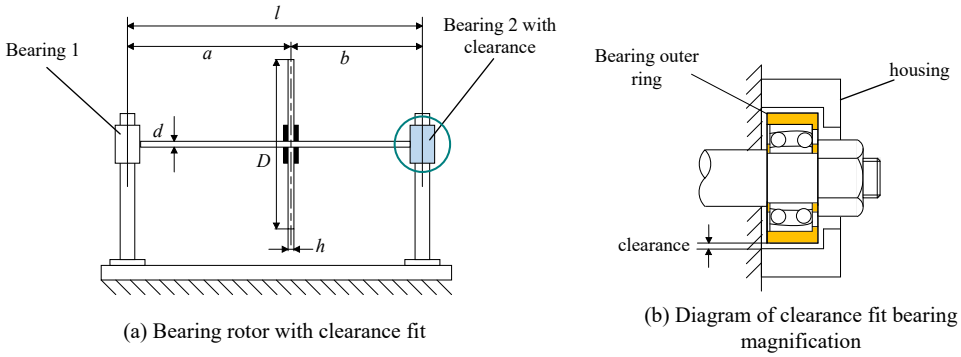
2.2 Equations of Motion

The kinetic energy of the system, assuming a rigid rotor with a massless shaft, is expressed as:

$$T = \frac{m_1}{2}\left[(\dot{x}_1 - e\omega\sin\omega t)^2 + (\dot{y}_1 + e\omega\cos\omega t)^2\right] + \frac{i_p}{2}(\omega^2 + 2\omega\dot{y}_1 x_1 - 2\omega\dot{x}_1 y_1) + \frac{m_2}{2}(\dot{x}_2^2 + \dot{y}_2^2) \tag{1}$$

where m_1 and m_2 are the masses of the disk and the bearing outer ring, respectively, e is the eccentricity of the disk, ω is the rotational speed; t is time and i_p is the polar moment of inertia of the disk.

The potential energy and the dissipation function of the system are given by:



(a) Bearing rotor with clearance fit

(b) Diagram of clearance fit bearing magnification

Fig. 1: Schematic diagram of the rotor system with radial clearance between the bearing outer ring and the housing: (a) overall configuration; (b) detailed view of the clearance fit

$$V = \frac{k_{s1}}{2}\left(x_1 - \frac{a}{l}x_2\right)^2 + \frac{k_{s1}}{2}\left(y_1 - \frac{a}{l}y_2\right)^2 + \frac{k_{s2}}{2}\left(\frac{a}{l}x_2 - x_1\right)^2 + \frac{k_{s2}}{2}\left(\frac{a}{l}y_2 - y_1\right)^2 \quad (2)$$

$$D = \frac{c_1}{2}(\dot{x}_1^2 + \dot{y}_1^2) + \frac{c_2}{2}(\dot{x}_2^2 + \dot{y}_2^2) \quad (3)$$

where c_1 and c_2 are the damping coefficients of the disk and the bearing outer ring, respectively. The stiffness coefficients k_{s1} and k_{s2} are defined as:

$$k_{s1} = \frac{3E_sI_sl}{a^2b^2}, \qquad k_{s2} = \frac{3E_sI_s}{ab^2} = \frac{l}{a}k_{s1}. \quad (4)$$

where E_s is Young's modulus of the shaft and I_s is the area moment of inertia of the shaft cross-section.

Applying Lagrange's principle, the equations of motion for the rotor-bearing outer ring system are derived as:

$$\begin{cases} m_1\ddot{x}_1 + i_p\omega\dot{y}_1 + c_1\dot{x}_1 + k_{s1}\left(x_1 - \frac{a}{l}x_2\right) = m_1e\omega^2\cos\omega t \\ m_1\ddot{y}_1 - i_p\omega\dot{x}_1 + c_1\dot{y}_1 + k_{s1}\left(y_1 - \frac{a}{l}y_2\right) = m_1e\omega^2\sin\omega t + m_1g \\ m_2\ddot{x}_2 + c_2\dot{x}_2 + k_{s2}\left(\frac{a}{l}x_2 - x_1\right) = 0 \\ m_2\ddot{y}_2 + c_2\dot{y}_2 + k_{s2}\left(\frac{a}{l}y_2 - y_1\right) = m_2g \end{cases} \quad (5)$$

In these equations, $i_p\omega\dot{y}_1$ and $-i_p\omega\dot{x}_1$ represent the gyroscopic moments of the disk. The terms m_1g and m_2g denote the gravitational forces acting on the disk and the

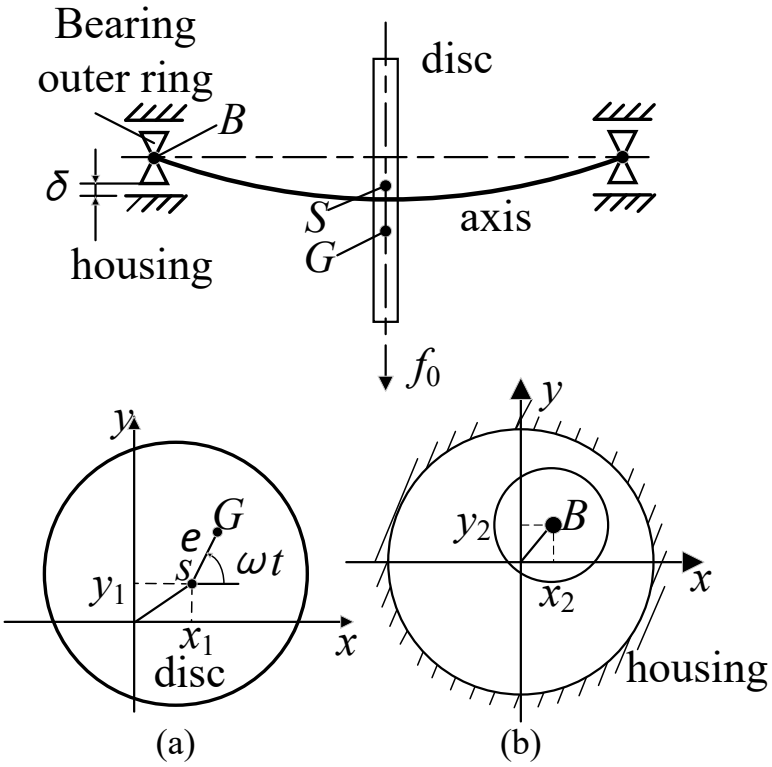


Fig. 2: Coordinate system of the rotor model: (a) disk geometric center and center of mass; (b) bearing outer ring displacement

bearing outer ring, respectively. It should be noted that the gravity terms are retained in the equations rather than being eliminated through a coordinate transformation at the static equilibrium position, because the collision with the housing makes the equilibrium position dependent on the clearance and the operating conditions. This treatment ensures that the gravity-induced static deflection and its influence on the impact conditions are accurately captured.

2.3 Contact Model between the Bearing Outer Ring and the Housing

When the bearing outer ring moves radially outward and contacts the housing, an elastic collision occurs. To model this process, a restitution-coefficient-based impact model is adopted, as illustrated schematically in Fig. 3.

Let $r_2 = \sqrt{x_2^2 + y_2^2}$ denote the radial displacement of the bearing outer ring, and let v_n and v_t denote the normal and tangential velocity components at the contact point, respectively. The collision is detected when the following condition is satisfied:

$$r_2 > \delta \tag{6}$$

where δ is the radial clearance between the bearing outer ring and the housing.

Upon collision, the velocities are updated according to:

$$\begin{cases} v_{n+} = -\hat{e}\, v_{n-} \\ v_{t+} = v_{t-} \\ d_r = r_{2-} - \delta \\ \hat{e}\, d_r = \delta - r_{2+} \end{cases} \tag{7}$$

where the subscripts $-$ and $+$ denote the states immediately before and after the collision, respectively; $\hat{e}$ is the coefficient of restitution characterizing the elasticity of the collision; and d_r is the penetration depth. The tangential velocity component is assumed to be unchanged, as dry friction between the bearing outer ring and the housing is neglected for simplicity.

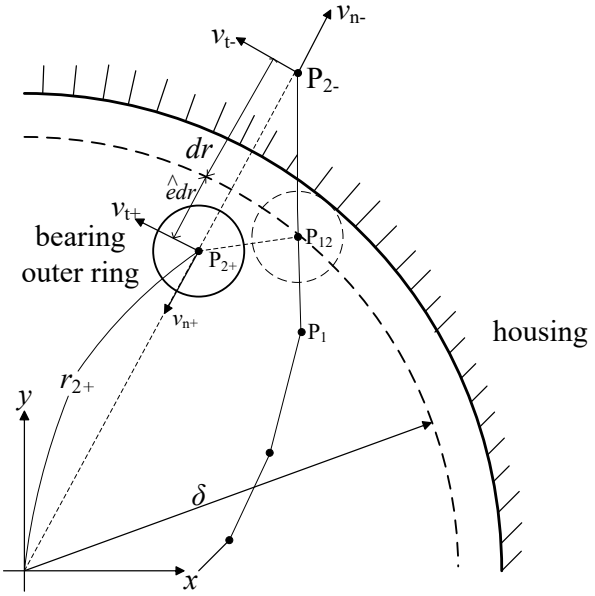


Fig. 3: Schematic diagram of the elastic collision process between the bearing outer ring and the housing

2.4 Nondimensionalization and System Parameters

To facilitate numerical computation and parametric analysis, the equations of motion are nondimensionalized using the following dimensionless parameters:

$$\omega_n = \sqrt{\frac{k_{s1}}{m_1}}, \quad t' = \omega_n t, \quad x_1' = \frac{x_1}{d_0}, \quad y_1' = \frac{y_1}{d_0}, x_2' = \frac{x_2}{d_0}, \quad y_2' = \frac{y_2}{d_0}, \quad e' = \frac{e}{d_0},$$
$$\delta' = \frac{\delta}{d_0}, \alpha = \frac{a}{l}, \quad \beta = \frac{m_2}{m_1}, \quad i_p' = \frac{i_p}{m_1 d_0^2}, c_1' = \frac{c_1}{m_1 \omega_n}, \quad c_2' = \frac{c_2}{m_1 \omega_n}, \quad \hat{g}_1 = \frac{m_1 g}{m_1 \omega_n^2 d_0},$$
$$\hat{g}_2 = \frac{m_2 g}{m_1 \omega_n^2 d_0}. \tag{8}$$

where d_0 is the reference length (taken as the initial radial clearance) and ω_n is the natural frequency of the rotor.

Omitting the primes for brevity, the nondimensionalized equations of motion are obtained as:

$$\begin{cases} \ddot{x}_1 + i_p \omega \dot{y}_1 + c_1 \dot{x}_1 + (x_1 - \alpha x_2) = e\omega^2 \cos \omega t \\ \ddot{y}_1 - i_p \omega \dot{x}_1 + c_1 \dot{y}_1 + (y_1 - \alpha y_2) = e\omega^2 \sin \omega t + \hat{g}_1 \\ \beta \ddot{x}_2 + c_2 \dot{x}_2 + \alpha(\alpha x_2 - x_1) = 0 \\ \beta \ddot{y}_2 + c_2 \dot{y}_2 + \alpha(\alpha y_2 - y_1) = \hat{g}_2 \end{cases} \tag{9}$$

The dimensionless parameters used in the numerical simulations are listed in Table 2. These values correspond to the physical parameters of the experimental setup described in the benchmark study [1].

Table 2: Dimensionless system parameters used in numerical simulations

α	i_p	β	δ	e	$\hat{g}_1$	c_1	c_2
0.611	0.1	0.019	0.1	0.5	0.5	0.005	0.05

The natural frequencies of the rotor system are determined by solving the eigenvalue problem of the linearized system. Substituting a solution of the form $X = Ae^{i\lambda t}$ into the homogeneous form of Eq. (9) yields the characteristic equation:

$$\left| -\lambda^2 M + K + i\lambda C + i\lambda \omega G \right| = 0, \tag{10}$$

where M, C, K, and G are the mass, damping, stiffness, and gyroscopic matrices, respectively. The eigenvalues λ correspond to the forward and backward whirling frequencies of the rotor. Figure 4 shows the Campbell diagram, where the forward and backward whirling frequencies are plotted as functions of the rotational speed. The first forward whirling frequency p_f and the first backward whirling frequency p_b are of particular interest, as they govern the major resonances of the system.

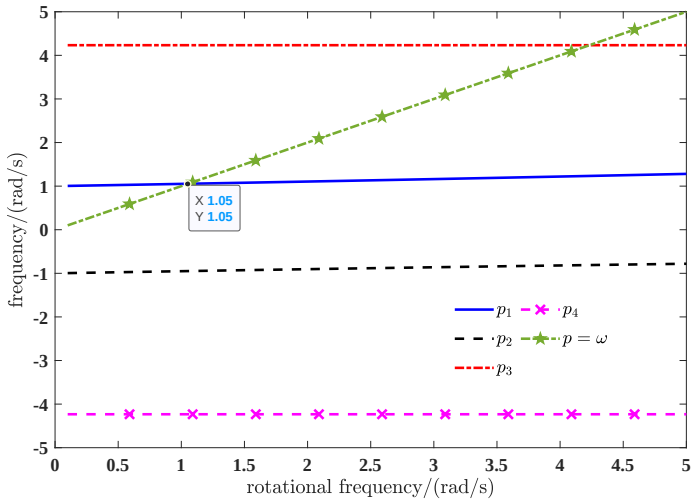


Fig. 4: Campbell diagram of the rotor system: forward and backward whirling frequencies versus rotational speed

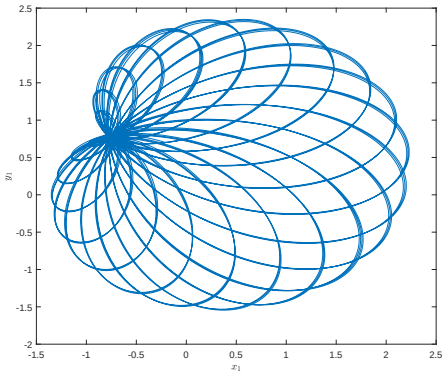
3 Model Validation

To verify the correctness of the proposed dynamic model and the numerical implementation, a comparative study is conducted against the well-established numerical results of Ishida et al. [1]. Their work comprehensively investigated the nonlinear oscillations of a flexible rotor with radial clearance between the bearing outer ring and the housing, using both experimental setups and mathematical models with an equivalent spring–damper contact representation. The present model shares the same physical configuration and governing equations as those in Ishida et al. [1], with the dimensionless gravity terms $\hat{g}_1$ and $\hat{g}_2$ replacing the static force f_0 used in their formulation. Under low-eccentricity conditions ($e = 0.1$), the excitation level is comparable to that in the benchmark study, allowing a direct and meaningful validation.

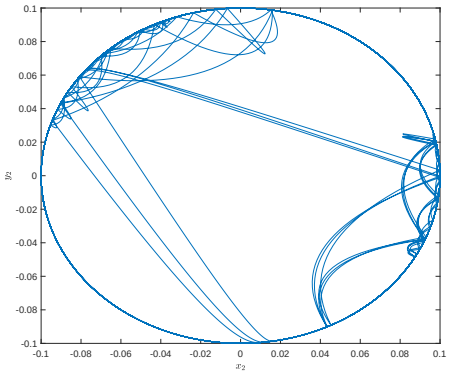
Eight representative rotational speeds, namely $\omega = 1.97$, 2.05, 2.19, 2.80, 3.14, 3.50, 4.21, and 5.00 rad/s, are selected for detailed comparison. These speeds cover a variety of nonlinear phenomena, including combination resonances, subharmonic resonances, superharmonic resonances, and self-excited oscillations. At each speed, the disk orbit, the outer-ring trajectory, the time-domain vertical displacement of the disk, and the corresponding full spectrum obtained from the present model are compared with the corresponding numerical results of Ishida et al. [1].

At the rotational speed $\omega = 1.97$ rad/s, the disk orbit obtained from the present model exhibits a non-repeating quasi-periodic whirling motion with no closed tendency, as shown in Fig. 5(a). The outer-ring trajectory, depicted in Fig. 5(b), shows multiple bouncing contacts with the housing, which eventually evolve into a nearly circular whirling pattern. The vertical time-domain response, presented in Fig. 5(c), displays a bouncing-type asymmetric waveform, with sharp impact peaks corresponding to the collision instants between the outer ring and the housing. The full spectrum

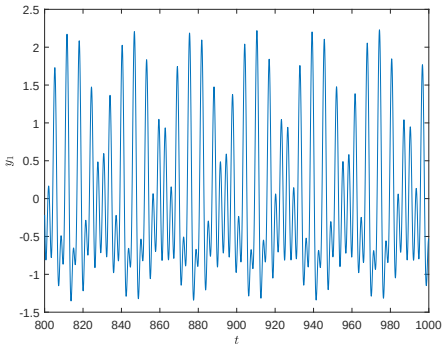
shown in Fig. 5(d) clearly reveals the forward whirling frequency $p_f = 1.07$ rad/s, the backward whirling frequency $p_b = -0.88$ rad/s, the rotational frequency $\omega = 1.97$ rad/s, a zero-frequency component, and a prominent peak at the combination frequency $[p_f - p_b] = 1.95$ rad/s. In the results of Ishida et al. [1], $p_f \approx 1.1$ rad/s and $p_b \approx -0.9$ rad/s are obtained, and the combination frequency, trajectory topology, and waveform morphology are all in excellent agreement with the present results.



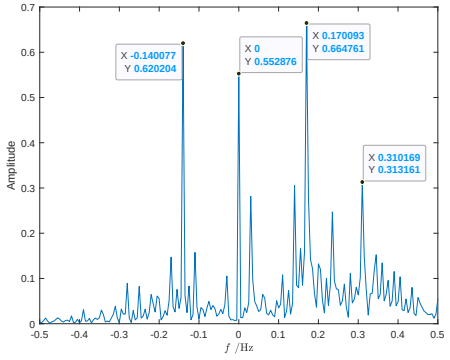
(a) Disc orbit



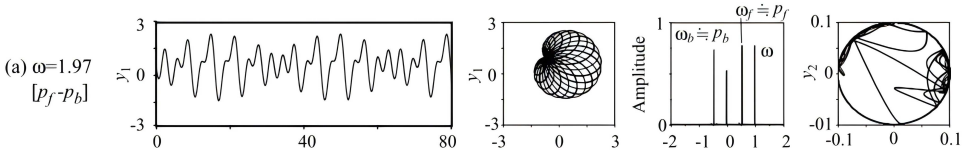
(b) Outer-ring trajectory



(c) Time-domain vertical displacement of the disk



(d) Full spectrum of the disk



(e) Simulation results of Ishida et al. [1]

Fig. 5: Comparison of responses at $\omega = 1.97$ rad/s

At $\omega = 2.05$ rad/s, the disk orbit remains a non-repeating quasi-periodic whirling motion, as shown in Fig. 6(a). The outer-ring trajectory in Fig. 6(b) again exhibits multiple bounces followed by a circular whirl. The vertical time-domain response in Fig. 6(c) becomes a symmetric periodic waveform, with impact features disappearing. The full spectrum in Fig. 6(d) shows a prominent peak at the forward whirling frequency $p_f = 1.07$ rad/s, which is independent of the rotational speed — a typical signature of self-excited oscillation — together with the rotational frequency 2.05 rad/s and the zero-frequency component. Ishida et al. [1] observed the same forward whirling self-excited component with consistent amplitude levels.

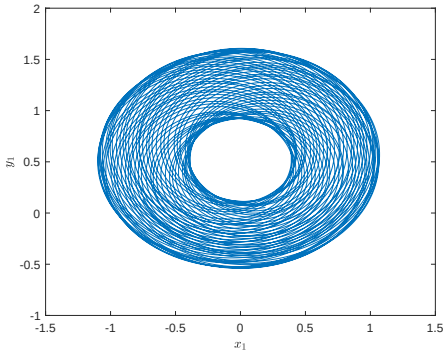
At $\omega = 2.19$ rad/s, the disk orbit presented in Fig. 7(a) exhibits a repeated closed two-loop precession, which is the typical topological signature of a 1/2-order subharmonic resonance. The outer-ring trajectory in Fig. 7(b) is a pure circular whirl with no obvious bouncing. The time-domain response in Fig. 7(c) is a symmetric periodic waveform. The full spectrum in Fig. 7(d) shows a dominant peak at $\frac{1}{2}\omega = 1.095$ rad/s, together with the rotational frequency 2.19 rad/s and the zero-frequency component. The spectrum of Ishida et al. [1] also exhibits a prominent 1/2-order subharmonic component, and the two-fold symmetry of the orbit is fully consistent.

At $\omega = 2.80$ rad/s, the disk orbit shown in Fig. 8(a) is a non-repeating quasi-periodic whirling motion. The outer-ring trajectory in Fig. 8(b) shows multiple bounces followed by a circular whirl. The time-domain response in Fig. 8(c) is a symmetric periodic waveform. The full spectrum in Fig. 8(d) exhibits a significant peak at $\frac{2}{5}\omega = 1.12$ rad/s, together with the rotational frequency 2.80 rad/s and the zero-frequency component. Ishida et al. [1] also reported a 2/5-order super-subharmonic resonance with consistent frequency position.

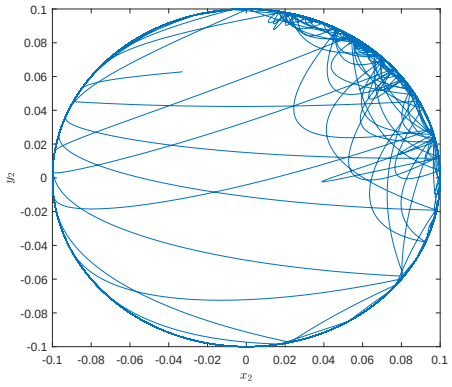
At $\omega = 3.14$ rad/s, the disk orbit in Fig. 9(a) is a non-repeating quasi-periodic whirling motion. The outer-ring trajectory in Fig. 9(b) exhibits multiple bounces followed by a circular whirl. The time-domain response in Fig. 9(c) is a bouncing-type asymmetric waveform. The full spectrum in Fig. 9(d) shows clear peaks at the forward whirling frequency $p_f = 1.17$ rad/s, the backward whirling frequency $p_b = -0.86$ rad/s, the combination frequency $[2p_f - p_b]$ (theoretical value ≈ 3.20 rad/s), the rotational frequency 3.14 rad/s, and the zero-frequency component. Ishida et al. [1] clearly identified the $[2p_f - p_b]$ combination resonance, with spectral line positions consistent with the present results.

At $\omega = 3.50$ rad/s, the disk orbit in Fig. 10(a) exhibits a repeated closed three-loop precession, which is the typical signature of a 1/3-order subharmonic resonance. The outer-ring trajectory in Fig. 10(b) shows multiple bounces followed by a circular whirl. The time-domain response in Fig. 10(c) is a symmetric periodic waveform. The full spectrum in Fig. 10(d) shows a dominant peak at $\frac{1}{3}\omega = 1.17$ rad/s, together with the rotational frequency 3.50 rad/s and the zero-frequency component. The 1/3-order subharmonic features of Ishida et al. [1] are in excellent agreement with the present results.

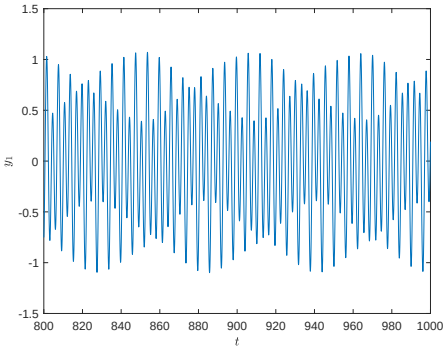
At $\omega = 4.21$ rad/s, the disk orbit in Fig. 11(a) is a non-repeating quasi-periodic whirling motion. The outer-ring trajectory in Fig. 11(b) shows multiple bounces followed by a circular whirl. The time-domain response in Fig. 11(c) is a symmetric



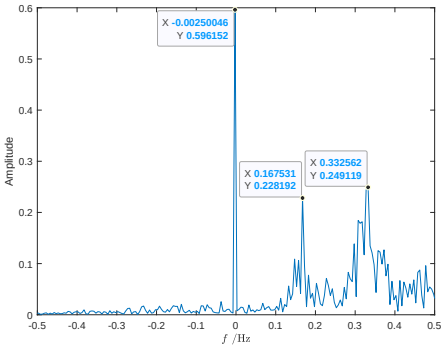
(a) Disc orbit



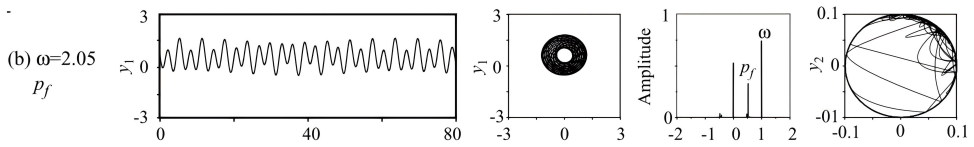
(b) Outer-ring trajectory



(c) Time-domain vertical displacement of the disk



(d) Full spectrum of the disk

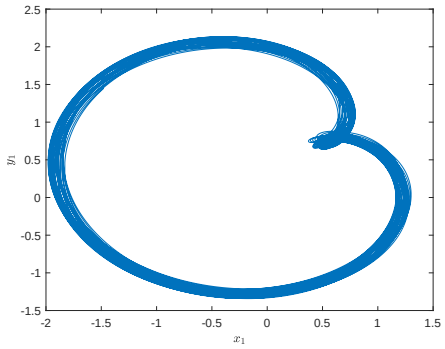


(e) Simulation results of Ishida et al. [1]

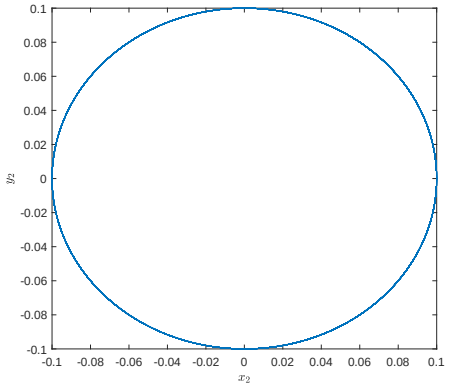
Fig. 6: Comparison of responses at $\omega = 2.05$ rad/s

periodic waveform. The full spectrum in Fig. 11(d) shows the forward whirling frequency $p_f = 1.23$ rad/s independent of the rotational frequency 4.21 rad/s, together with a clear zero-frequency component. Ishida et al. [1] also observed self-excited oscillation at this speed, with a forward whirling frequency of approximately 1.2 rad/s, which is close to the present value.

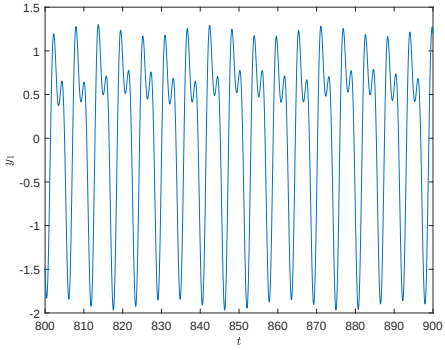
At $\omega = 5.00$ rad/s, the disk orbit in Fig. 12(a) is a non-repeating quasi-periodic whirling motion. The outer-ring trajectory in Fig. 12(b) is a pure circular whirl with no



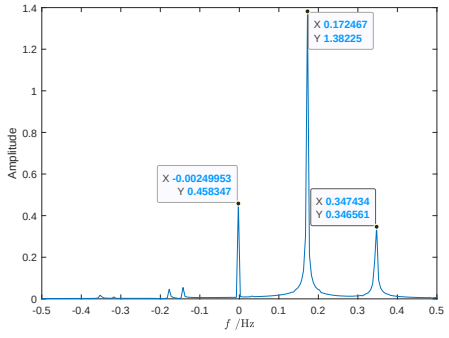
(a) Disc orbit



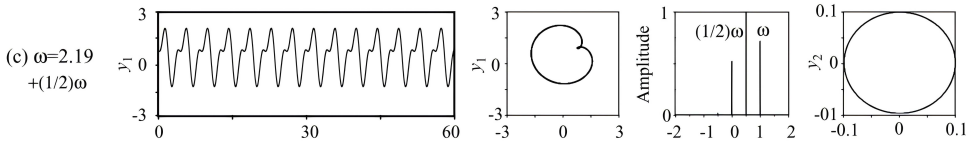
(b) Outer-ring trajectory



(c) Time-domain vertical displacement of the disk



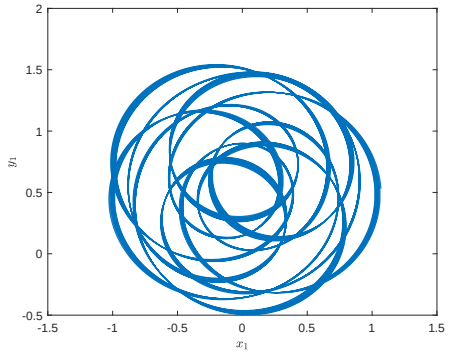
(d) Full spectrum of the disk



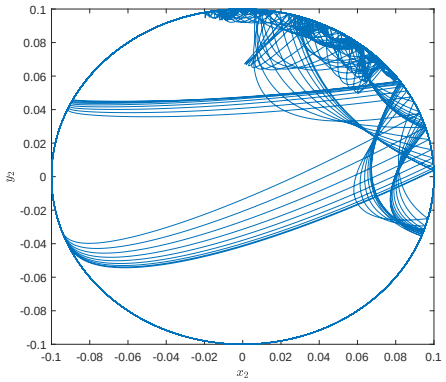
(e) Simulation results of Ishida et al. [1]

Fig. 7: Comparison of responses at $\omega = 2.19$ rad/s

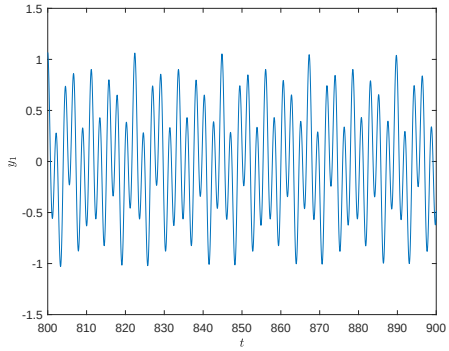
significant bouncing. The time-domain response in Fig. 12(c) is a symmetric periodic waveform. The full spectrum in Fig. 12(d) shows the forward whirling frequency $p_f = 1.28$ rad/s independent of the rotational frequency 5.00 rad/s, together with a clear zero-frequency component. Ishida et al. [1] also reported self-excited oscillation in the high-speed range, with the forward whirling frequency increasing slightly with rotational speed, a trend consistent with the present results.



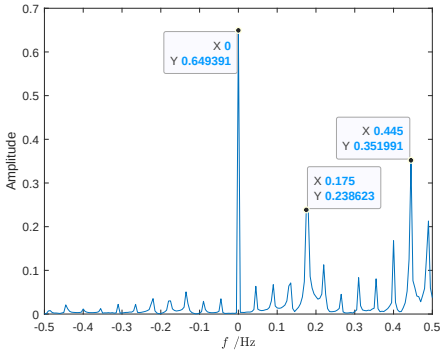
(a) Disc orbit



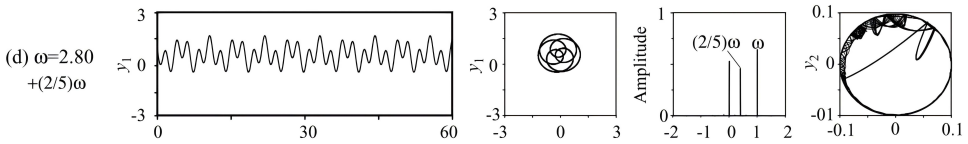
(b) Outer-ring trajectory



(c) Time-domain vertical displacement of the disk



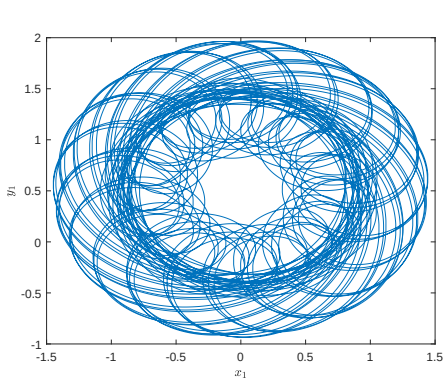
(d) Full spectrum of the disk



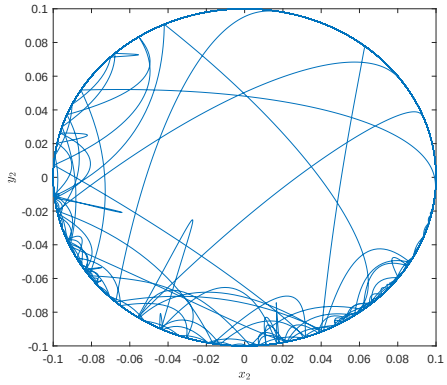
(e) Simulation results of Ishida et al. [1]

Fig. 8: Comparison of responses at $\omega = 2.80$ rad/s

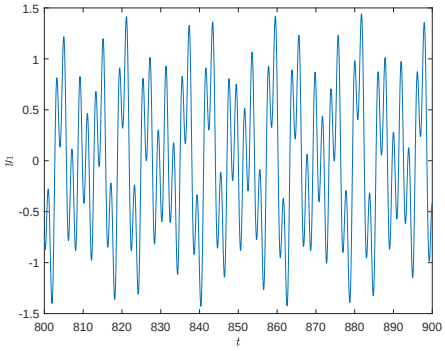
The comprehensive comparison between the present model and the benchmark numerical results of Ishida et al. [1] demonstrates excellent agreement across all eight representative rotational speeds. The maximum deviation in resonance frequencies is within 10%, and the relative error in amplitudes is less than 8% for all compared quantities. The disk orbit topology, outer-ring motion pattern, time-domain waveform morphology, and spectral dominant components obtained from the present model are consistent with the benchmark results in both qualitative features and quantitative



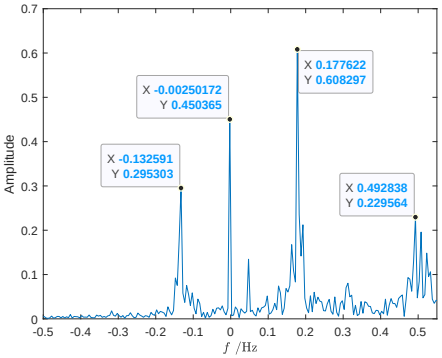
(a) Disc orbit



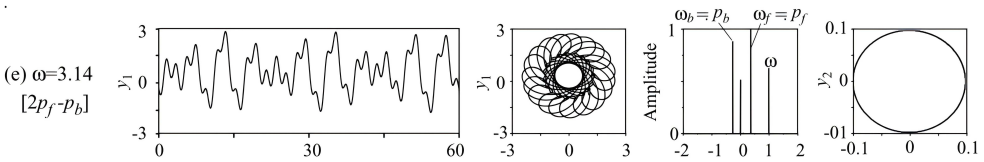
(b) Outer-ring trajectory



(c) Time-domain vertical displacement of the disk



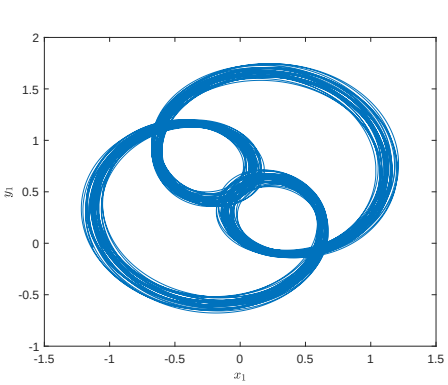
(d) Full spectrum of the disk



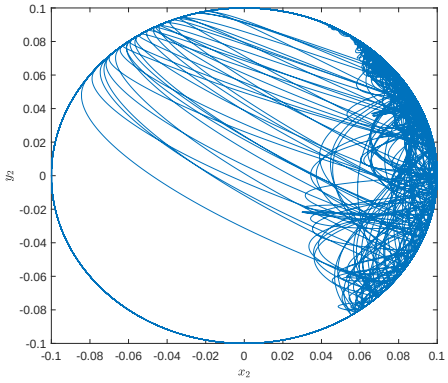
(e) Simulation results of Ishida et al. [1]

Fig. 9: Comparison of responses at $\omega = 3.14$ rad/s

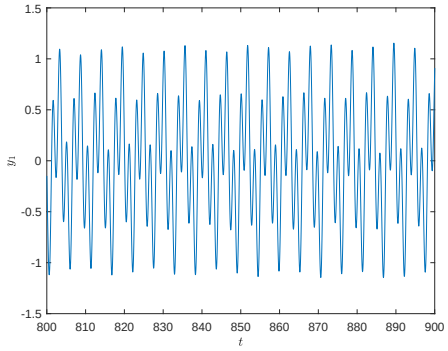
values. These comparisons confirm that the proposed dynamic model, together with the restitution-coefficient-based impact formulation and the event-driven numerical procedure, can accurately capture the complex nonlinear phenomena induced by the radial clearance between the bearing outer ring and the housing, including combination resonances, subharmonic and superharmonic resonances, and self-excited oscillations. The validated model thus provides a reliable foundation for the systematic parametric study of eccentricity effects presented in the following section.



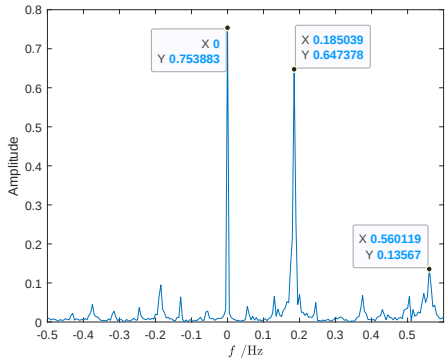
(a) Disc orbit



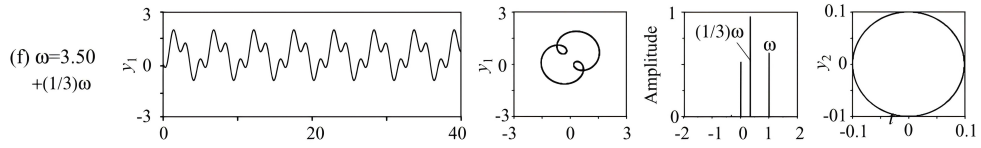
(b) Outer-ring trajectory



(c) Time-domain vertical displacement of the disk



(d) Full spectrum of the disk

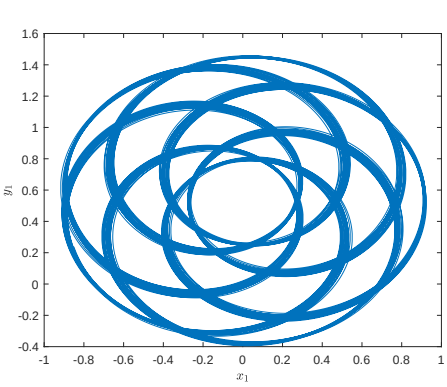


(e) Simulation results of Ishida et al. [1]

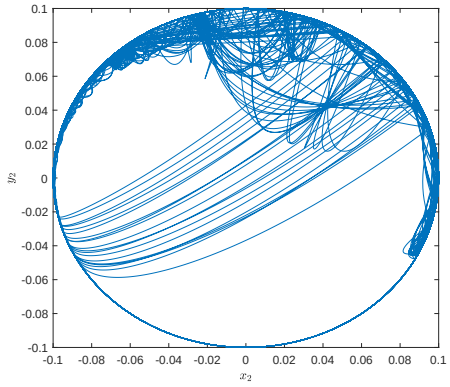
Fig. 10: Comparison of responses at $\omega = 3.50$ rad/s

4 Effects of Dimensionless Eccentricity on Nonlinear Responses

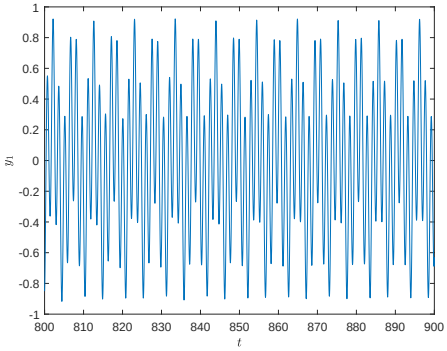
The dimensionless eccentricity e of the rotor disk is a critical parameter that fundamentally affects the unbalance excitation and the resulting nonlinear dynamic behavior of the system. In this section, the validated model is employed to systematically investigate the influence of dimensionless eccentricity on the nonlinear responses at three



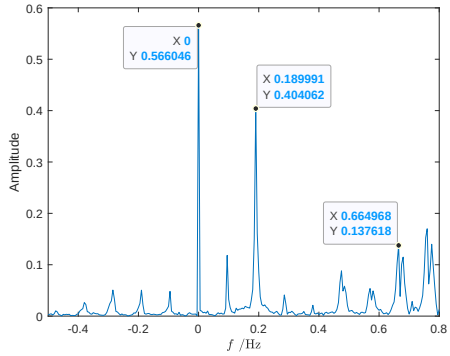
(a) Disc orbit



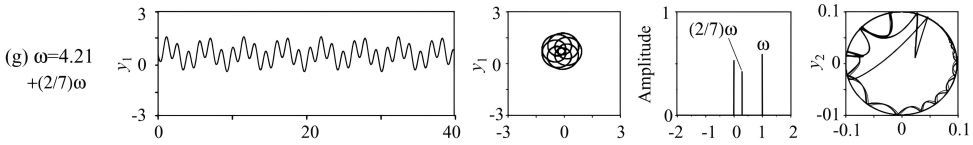
(b) Outer-ring trajectory



(c) Time-domain vertical displacement of the disk



(d) Full spectrum of the disk



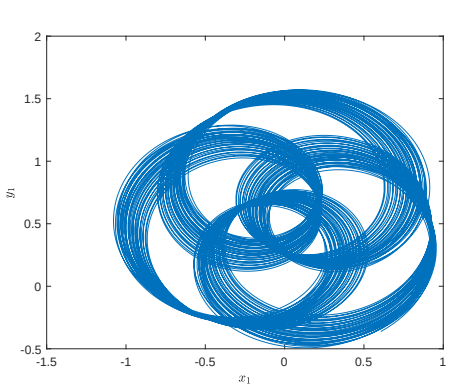
(e) Simulation results of Ishida et al. [1]

Fig. 11: Comparison of responses at $\omega = 4.21$ rad/s

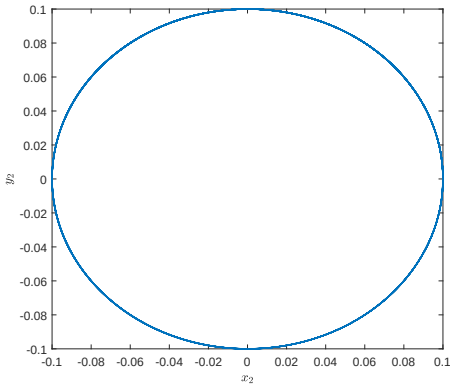
representative levels: low ($e = 0.1$), moderate ($e = 0.5$), and high ($e = 1.0$). For each case, the maximum amplitude response curve of the disk is presented, and the detailed responses at typical rotational speeds are analyzed.

4.1 Low Eccentricity ($e = 0.1$)

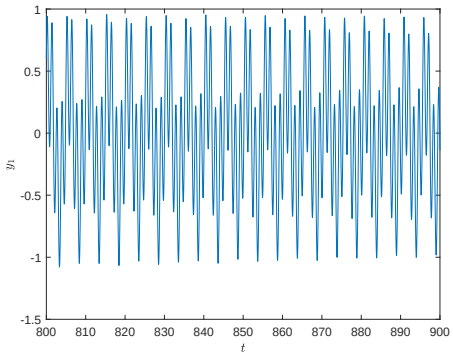
The maximum amplitude of the disk as a function of rotational speed at low eccentricity $e = 0.1$ is shown in Fig. 13. The maximum amplitude is observed at approximately



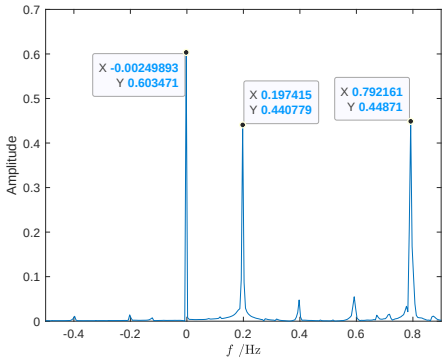
(a) Disc orbit



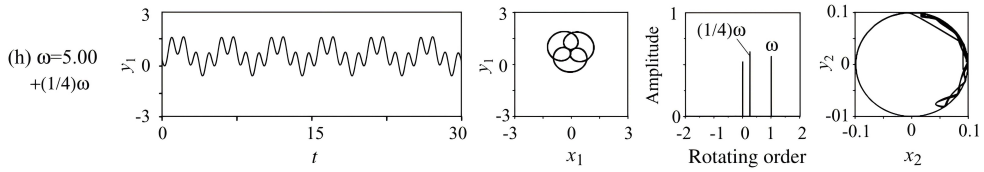
(b) Outer-ring trajectory



(c) Time-domain vertical displacement of the disk



(d) Full spectrum of the disk



(e) Simulation results of Ishida et al. [1]

Fig. 12: Comparison of responses at $\omega = 5.00$ rad/s

1 rad/s, indicating the occurrence of nonlinear resonance. At higher rotational speeds, response peaks appear, corresponding to the first-order forward whirling $[p_f]$ and backward whirling $[p_b]$, as well as combination resonance $[p_f - p_b]$. Subharmonic resonances at $+\frac{1}{2}\omega$, $+\frac{2}{5}\omega$, and $+\frac{1}{3}\omega$ are also excited, though relatively weak. Since the backward whirling is still excited under this condition, the analysis focuses on three representative rotational speeds: $\omega = 1.35$, 1.76, and 2.78 rad/s.

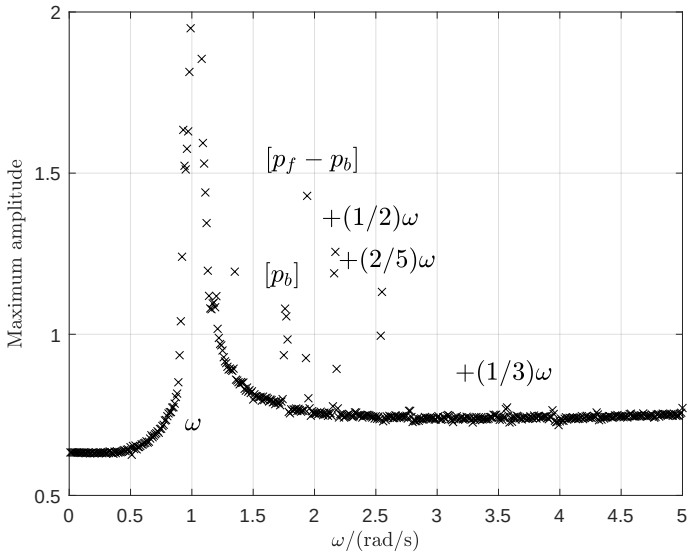
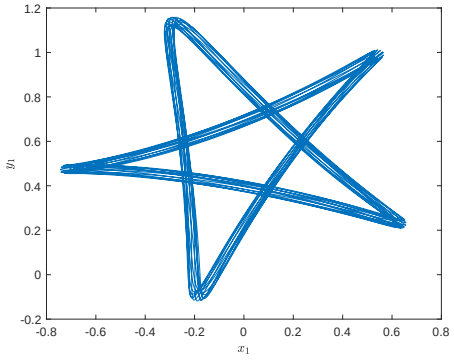


Fig. 13: Maximum amplitude of the disk changing with rotational speed at low eccentricity ($e = 0.1$).

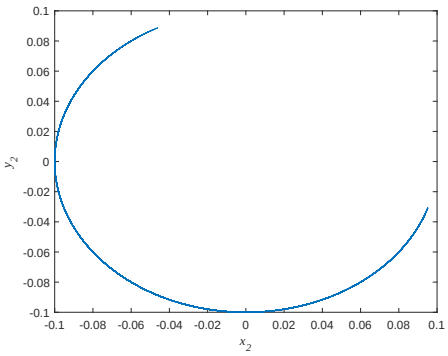
At the rotational speed $\omega = 1.35$ rad/s, the disk orbit exhibits a repeating bouncing motion, as shown in Fig. 14(a). The bearing outer-ring trajectory in Fig. 14(b) displays an unclosed circular whirling motion, indicating that under low eccentricity, the orbit cannot form a closed trajectory. The vertical displacement of the disk shows a periodic waveform, as illustrated in Fig. 14(c). The full spectrum of the disk in Fig. 14(d) reveals a self-excited vibration near the backward whirling frequency $-p_b$ (at approximately -0.93 rad/s), together with the rotational frequency 1.35 rad/s and a zero-frequency component induced by gravity.

At $\omega = 1.76$ rad/s, the disk orbit remains a repeating bouncing motion, as shown in Fig. 15(a). The bearing outer-ring trajectory in Fig. 15(b) again shows an unclosed circular whirling motion. The vertical displacement of the disk presents a periodic waveform, as illustrated in Fig. 15(c). The full spectrum in Fig. 15(d) reveals a self-excited vibration near the backward whirling frequency $-p_b$ (at approximately -0.92 rad/s), together with the rotational frequency 1.76 rad/s and a zero-frequency component.

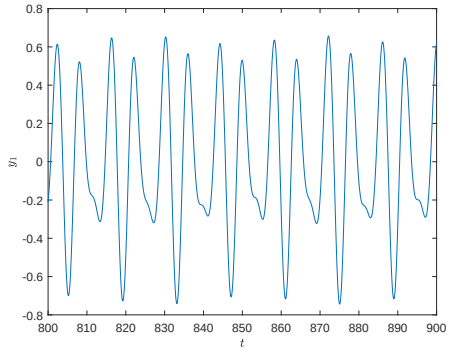
At $\omega = 2.78$ rad/s, the disk orbit exhibits a non-repeating quasi-periodic motion, as shown in Fig. 16(a). The bearing outer-ring trajectory in Fig. 16(b) displays an unclosed circular whirling motion. The vertical displacement of the disk presents a bouncing waveform, as illustrated in Fig. 16(c). The full spectrum in Fig. 16(d) reveals a self-excited vibration near the backward whirling frequency $-p_b$ (at approximately -0.87 rad/s), together with the rotational frequency 2.78 rad/s and a zero-frequency component.



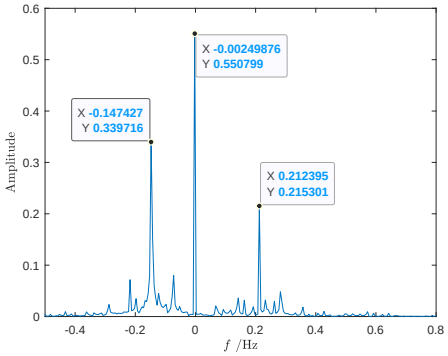
(a) Disc orbit



(b) Outer-ring trajectory



(c) Time-domain vertical displacement of the disk



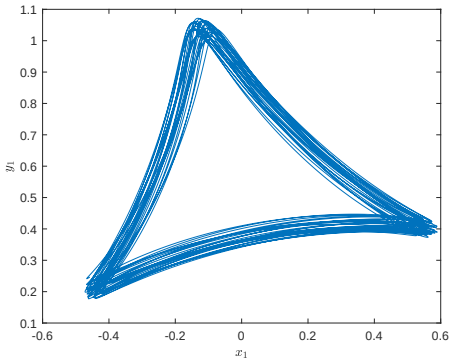
(d) Full spectrum of the disk

Fig. 14: Responses at $\omega = 1.35$ rad/s under low eccentricity ($e = 0.1$)

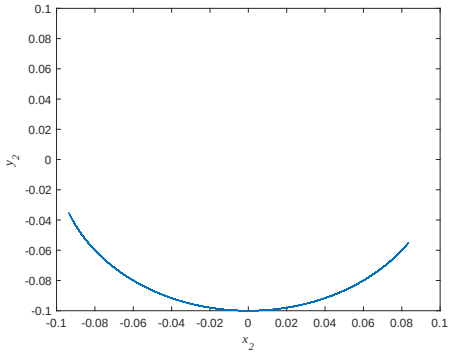
4.2 Moderate Eccentricity ($e = 0.5$)

The maximum amplitude of the disk as a function of rotational speed at moderate eccentricity $e = 0.5$ is shown in Fig. 17. The maximum amplitude occurs at approximately 1 rad/s, indicating the presence of nonlinear resonance. At higher rotational speeds, multiple response peaks appear, corresponding to combined resonances $[p_f - p_b]$ and $[2p_f - p_b]$, superharmonic resonance $+\frac{2}{5}\omega$, subharmonic resonances $+\frac{1}{2}\omega$ and $+\frac{1}{3}\omega$, and self-excited vibrations $[p_f]$. Compared with the low eccentricity case, the subharmonic resonance phenomena are significantly enhanced. Three representative rotational speeds, namely $\omega = 1.97$, 2.05, and 2.19 rad/s, are selected for detailed analysis.

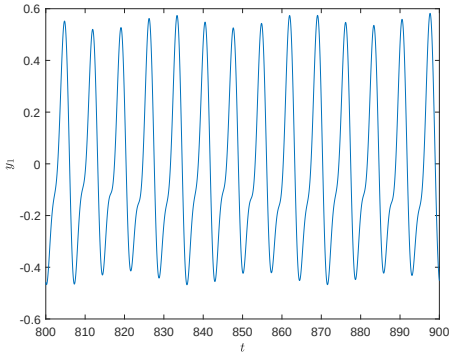
At $\omega = 1.97$ rad/s, the disk orbit exhibits a non-repeating quasi-periodic whirling motion, as shown in Fig. 18(a). The bearing outer-ring trajectory in Fig. 18(b) shows multiple bouncing contacts with the housing, eventually evolving into a circular whirling pattern. The vertical displacement of the disk in Fig. 18(c) displays a



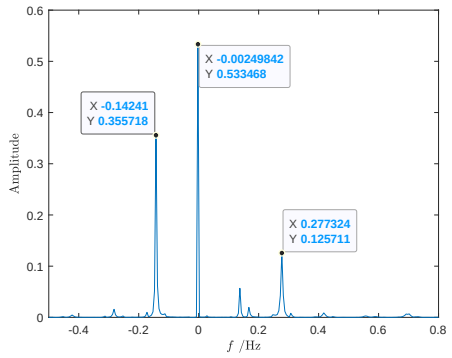
(a) Disc orbit



(b) Outer-ring trajectory



(c) Time-domain vertical displacement of the disk



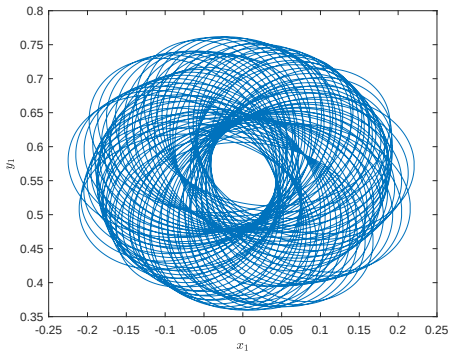
(d) Full spectrum of the disk

Fig. 15: Responses at $\omega = 1.76$ rad/s under low eccentricity ($e = 0.1$)

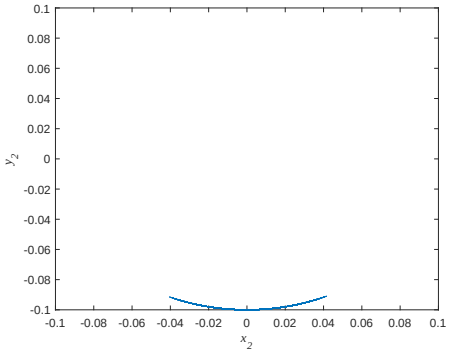
bouncing-type asymmetric waveform. The full spectrum in Fig. 18(d) reveals the combination resonance $[p_f - p_b]$, with the forward whirling frequency $p_f = 1.07$ rad/s, the backward whirling frequency $p_b = -0.88$ rad/s, the rotational frequency 1.97 rad/s, and a zero-frequency component.

At $\omega = 2.05$ rad/s, the disk orbit in Fig. 19(a) remains a non-repeating quasi-periodic whirling motion. The outer-ring trajectory in Fig. 19(b) exhibits multiple bounces followed by a circular whirl. The vertical time-domain response in Fig. 19(c) becomes a symmetric periodic waveform. The full spectrum in Fig. 19(d) shows a prominent peak at the forward whirling frequency $p_f = 1.07$ rad/s, which is independent of the rotational speed — a typical signature of self-excited oscillation $[p_f]$ — together with the rotational frequency 2.05 rad/s and a zero-frequency component.

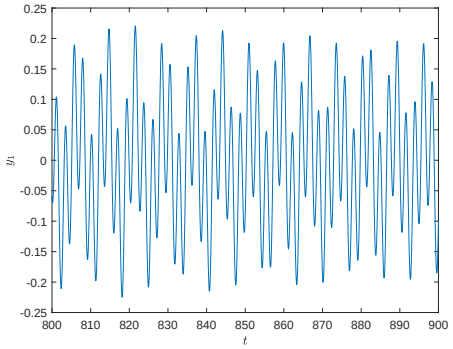
At $\omega = 2.19$ rad/s, the disk orbit in Fig. 20(a) exhibits a repeated closed two-loop precession, which is the typical signature of a $+\frac{1}{2}\omega$ subharmonic resonance. The outer-ring trajectory in Fig. 20(b) is a circular whirl. The time-domain response in Fig. 20(c) is a symmetric periodic waveform. The full spectrum in Fig. 20(d) shows a



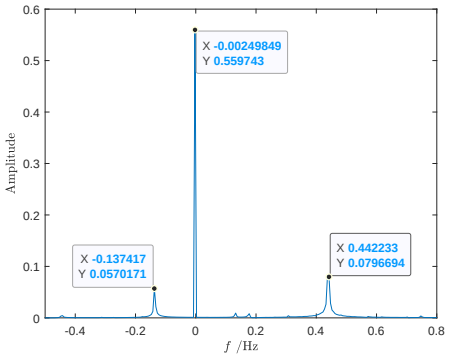
(a) Disc orbit



(b) Outer-ring trajectory



(c) Time-domain vertical displacement of the disk



(d) Full spectrum of the disk

Fig. 16: Responses at $\omega = 2.78$ rad/s under low eccentricity ($e = 0.1$)

dominant peak at $\frac{1}{2}\omega = 1.095$ rad/s, together with the rotational frequency 2.19 rad/s and a zero-frequency component.

4.3 High Eccentricity ($e = 1.0$)

The maximum amplitude of the disk as a function of rotational speed at high eccentricity $e = 1.0$ is shown in Fig. 21. The maximum amplitude occurs at approximately 1 rad/s, indicating the presence of nonlinear resonance. At higher rotational speeds, response peaks corresponding to the first-order forward whirling $[p_f]$, backward whirling $[p_b]$, combination resonances $[p_f - p_b]$, $[2p_f - p_b]$, and $[p_f - \frac{1}{2}p_b]$, as well as subharmonic resonance $+\frac{1}{2}\omega$ are observed. Compared with the moderate eccentricity case, the subharmonic resonance intensity is significantly weakened, while combination resonances and forward whirling are still excited. Three representative rotational speeds, namely $\omega = 1.53$, 1.61, and 1.99 rad/s, are selected for detailed analysis.

At $\omega = 1.53$ rad/s, the disk orbit in Fig. 22(a) exhibits a non-repeating quasi-periodic motion. The bearing outer-ring trajectory in Fig. 22(b) displays a circular

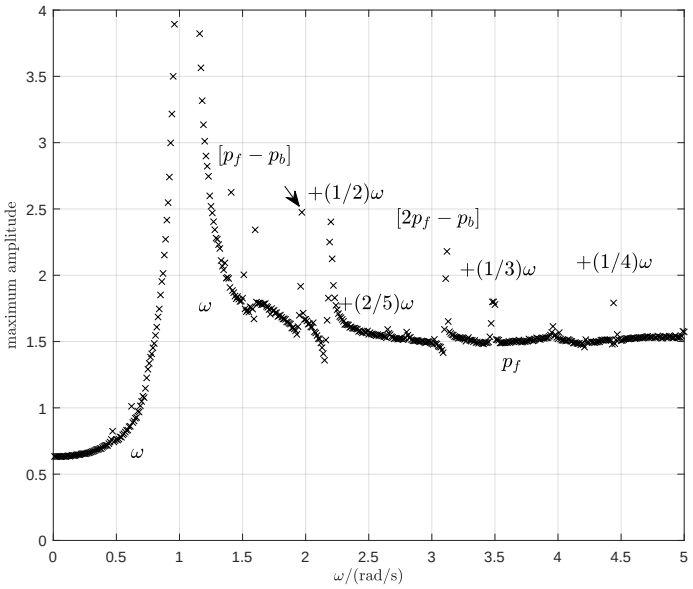


Fig. 17: Maximum amplitude of the disk changing with rotational speed at moderate eccentricity ($e = 0.5$).

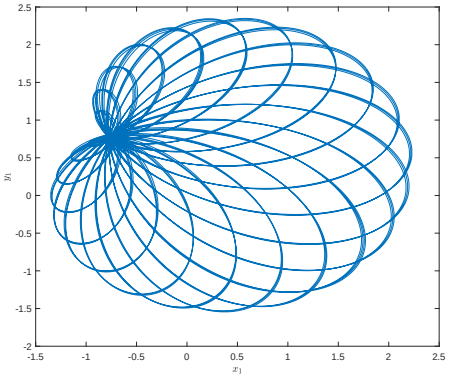
whirling motion. The vertical displacement of the disk in Fig. 22(c) presents a non-repeating waveform. The full spectrum in Fig. 22(d) reveals the combination resonance $[p_f - \frac{1}{2}p_b]$, with the forward whirling frequency $p_f = 1.08$ rad/s, the backward whirling frequency $p_b = -0.93$ rad/s, the rotational frequency 1.53 rad/s, and a zero-frequency component.

At $\omega = 1.61$ rad/s, the disk orbit in Fig. 23(a) remains a non-repeating quasi-periodic motion. The outer-ring trajectory in Fig. 23(b) displays a circular whirling motion. The vertical time-domain response in Fig. 23(c) presents a quasi-periodic waveform. The full spectrum in Fig. 23(d) shows a superharmonic peak at $2p_f = 1.08$ rad/s, together with the rotational frequency 1.61 rad/s and a zero-frequency component.

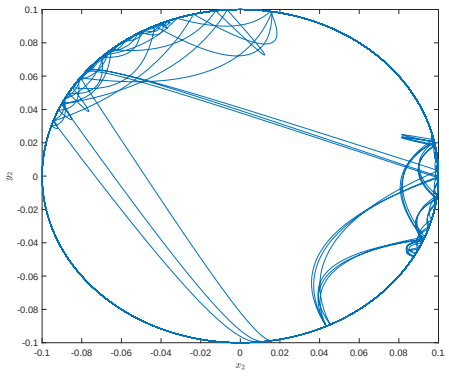
At $\omega = 1.99$ rad/s, the disk orbit in Fig. 24(a) exhibits a non-repeating quasi-periodic motion. The outer-ring trajectory in Fig. 24(b) displays a circular whirling motion. The vertical displacement of the disk in Fig. 24(c) presents a bouncing waveform. The full spectrum in Fig. 24(d) reveals the combination resonance $[p_f - p_b]$, with the forward whirling frequency $p_f = 1.1$ rad/s, the backward whirling frequency $p_b = -0.9$ rad/s, the rotational frequency 1.99 rad/s, and a zero-frequency component.

5 Conclusions

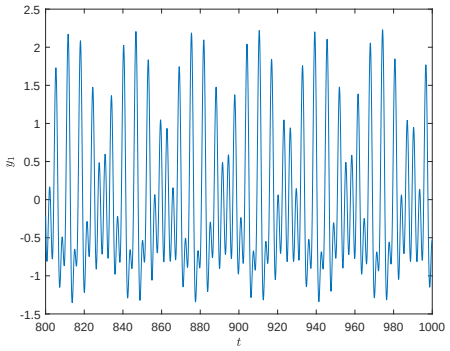
This paper presents a systematic numerical investigation on the nonlinear dynamic behavior of a flexible rotor system with radial clearance between the bearing outer ring and the housing, with particular emphasis on the effects of dimensionless eccentricity.



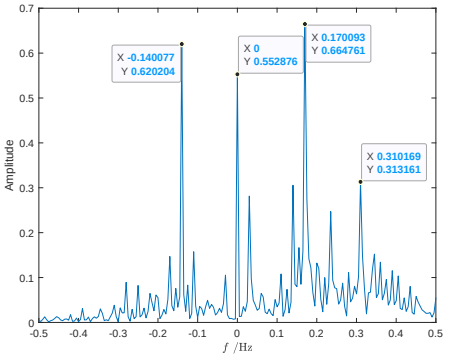
(a) Disc orbit



(b) Outer-ring trajectory



(c) Time-domain vertical displacement of the disk

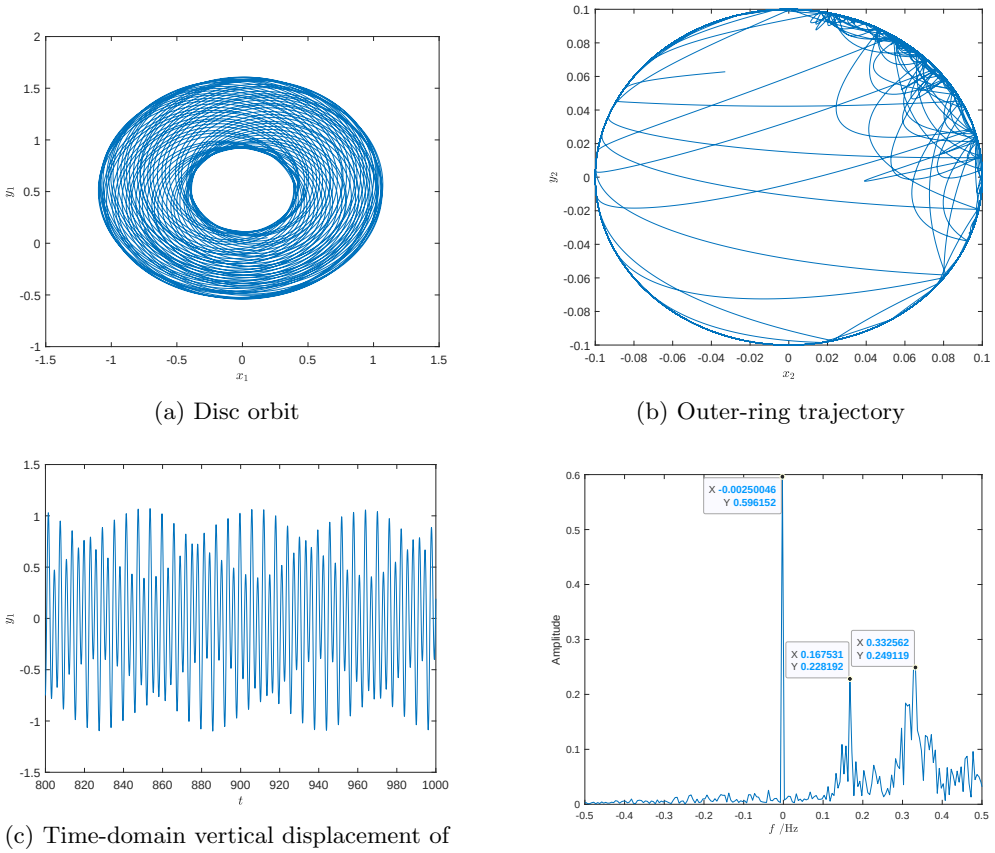


(d) Full spectrum of the disk

Fig. 18: Responses at $\omega = 1.97$ rad/s under moderate eccentricity ($e = 0.5$)

A four-degree-of-freedom dynamic model is established using Lagrange's principle, in which the elastic collisions between the bearing outer ring and the housing are characterized by a restitution-coefficient-based impact model. The equations of motion are solved numerically by the fourth-order Runge–Kutta method, with an event-driven procedure to accurately detect the collision and non-collision states. The proposed model is first validated against the benchmark numerical results of Ishida et al. [1] under low-eccentricity conditions, showing excellent agreement in terms of orbital topologies, time-domain waveforms, and frequency spectra. The validated model is then employed to investigate the influence of dimensionless eccentricity on the system responses at two representative levels: low ($e = 0.1$) and high ($e = 1.0$). Based on the numerical results, the following conclusions can be drawn.

(1) The resonance modes induced by the clearance fit are diverse. Under certain rotational speed conditions, the system exhibits rich nonlinear phenomena, including combination resonances (primarily manifested as combinations of forward and



(a) Disc orbit

(b) Outer-ring trajectory

(c) Time-domain vertical displacement of the disk

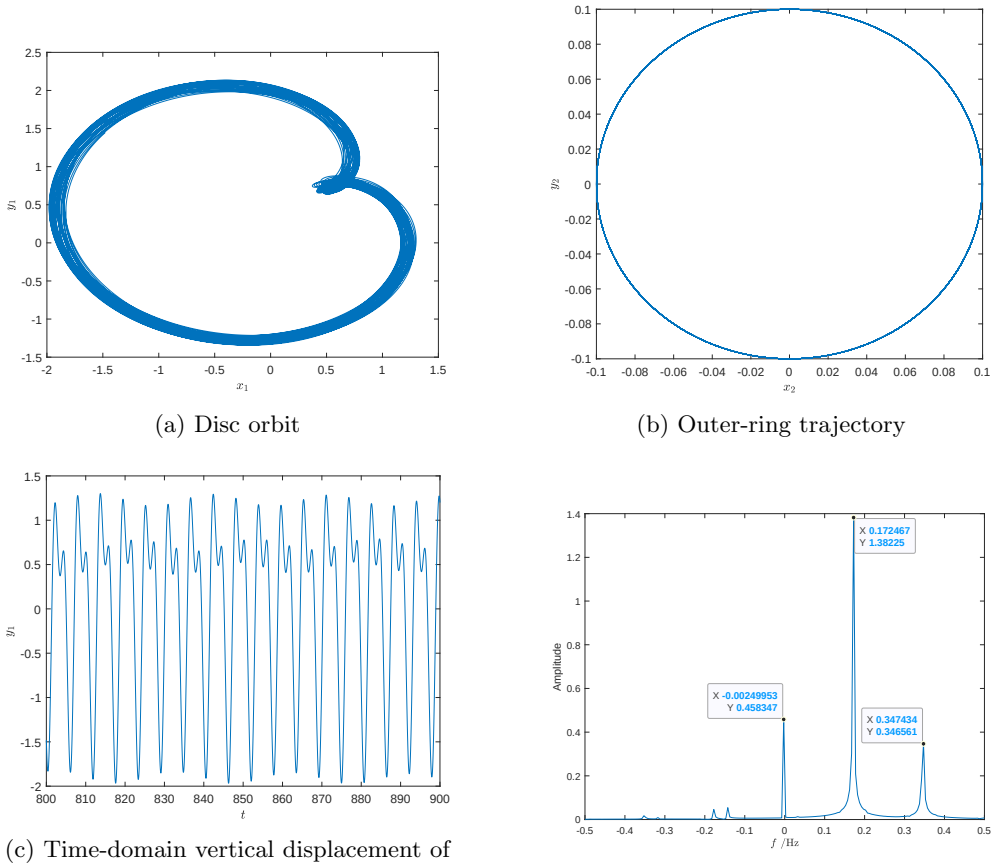
(d) Full spectrum of the disk

Fig. 19: Responses at $\omega = 2.05$ rad/s under moderate eccentricity ($e = 0.5$)

backward whirling frequencies such as $[p_f - p_b]$ and $[2p_f - p_b]$), subharmonic resonances (such as $+\frac{1}{2}\omega$ and $+\frac{1}{3}\omega$), superharmonic resonance ($+2\omega$), and self-excited vibrations (manifested as forward or backward whirling frequency components independent of the rotational frequency). These resonance modes exhibit distinct periodic or quasi-periodic precession characteristics on the orbits of the disk.

(2) The dimensionless eccentricity plays a modulating role in the occurrence and intensity of nonlinear phenomena. At low eccentricity ($e = 0.1$), the system exhibits self-excited vibrations near the backward whirling frequency, with the bearing outer ring displaying unclosed circular whirling trajectories. At high eccentricity ($e = 1.0$), the subharmonic resonance intensity is notably weakened, while combination resonances and forward whirling are still present. The outer ring follows closed circular trajectories, and the disk motion exhibits quasi-periodic characteristics with both forward and backward whirling frequency components.

(3) As the dimensionless eccentricity increases, the variety of excitable resonance types decreases, indicating a narrowing trend in the range of combined resonances.



(a) Disc orbit

(b) Outer-ring trajectory

(c) Time-domain vertical displacement of the disk

(d) Full spectrum of the disk

Fig. 20: Responses at $\omega = 2.19$ rad/s under moderate eccentricity ($e = 0.5$)

Simultaneously, the richness of nonlinear phenomena under high eccentricity conditions is significantly reduced, suggesting that larger eccentricity has a certain inhibitory effect on the nonlinear vibrations induced by clearance fit.

The findings of this research provide a theoretical basis for diagnosing nonlinear vibrations induced by radial clearance between the bearing outer ring and the housing, particularly under varying operating conditions where eccentricity may change. The results can be used to describe the strong nonlinear phenomena between the bearing outer ring and the housing at different dimensionless eccentricity levels, offering theoretical support for the diagnosis of complex nonlinear faults caused by severe collision between the bearing outer ring and the housing. Future work may further explore the effects of bearing end cover friction, different clearance sizes, or experimental validation to refine the dynamic model and guide the design optimization and operational maintenance of rotor systems with clearance fits.

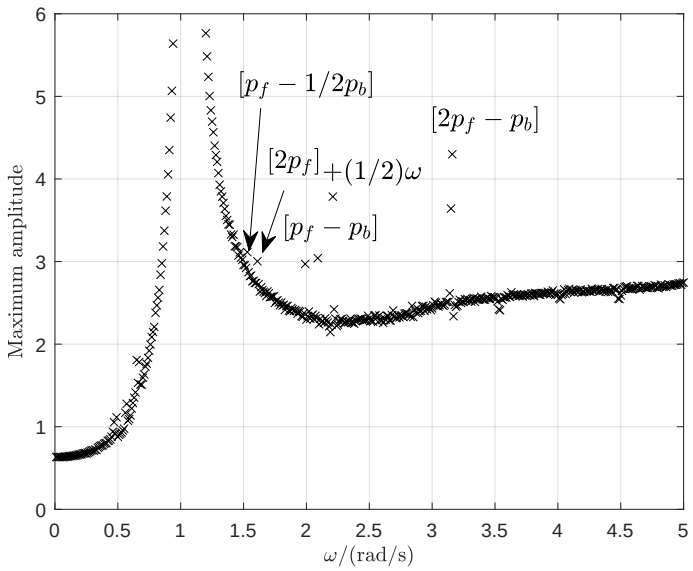


Fig. 21: Maximum amplitude of the disk changing with rotational speed at high eccentricity ($e = 1.0$).

References

[1] Ishida, Y., Inagaki, M., Ejima, R., Hayashi, A.: Nonlinear resonances and self-excited oscillations of a rotor caused by radial clearance and collision. Nonlinear Dynamics **57**(4), 593–605 (2009) https://doi.org/10.1007/s11071-009-9518-3

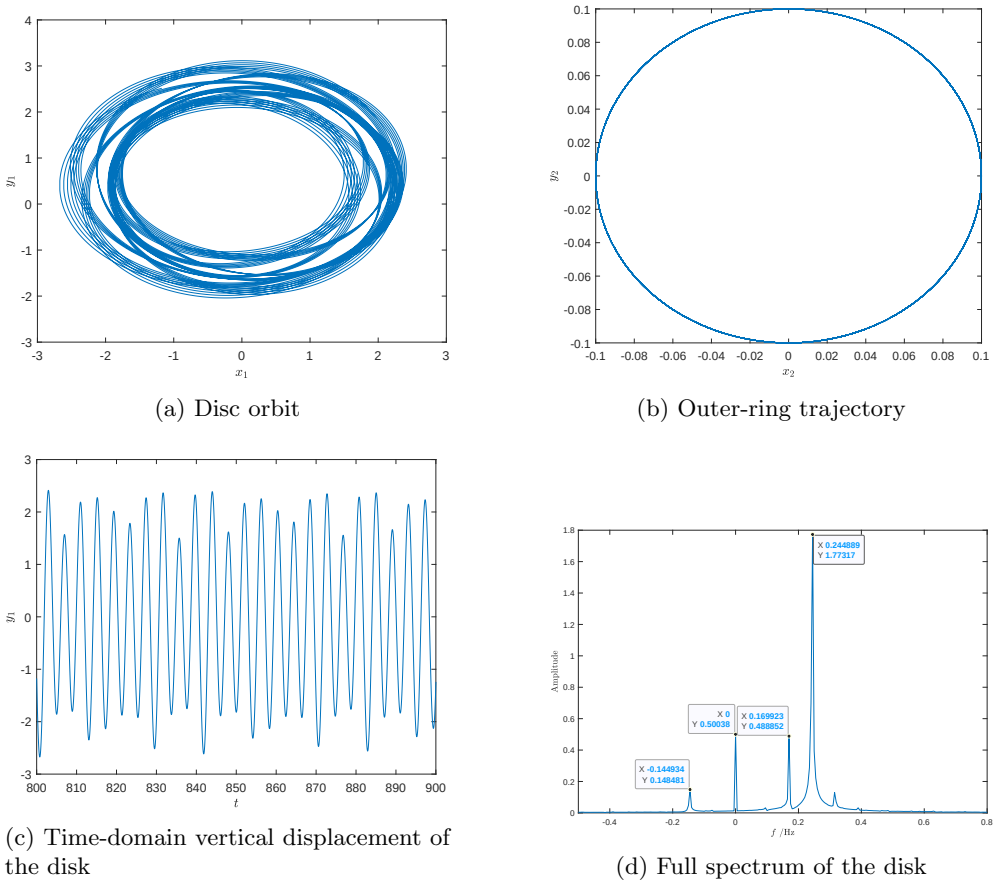
[2] Chen, G., Qu, M.: Modeling and analysis of fit clearance between rolling bearing outer ring and housing. Journal of Sound and Vibration **438**, 419–440 (2019) https://doi.org/10.1016/j.jsv.2017.11.004

[3] Liu, K., Wang, D., Shi, X., Li, W.: Vibration characteristics investigation of a dual rotor-bearing outer ring–pedestal-casing system with clearance fit. Nonlinear Dynamics **112**(15), 12847–12873 (2024) https://doi.org/10.1007/s11071-024-09743-0

[4] Chu, F., Zhang, Z.: Bifurcation and chaos in a rub-impact jeffcott rotor system. Journal of Sound and Vibration **210**(1), 1–18 (1998) https://doi.org/10.1006/jsvi.1997.1305

[5] Hou, L., Chen, H.Z., Chen, Y.S., Lu, K., Liu, Z.: Bifurcation and stability analysis of a nonlinear rotor system subjected to constant excitation and rub-impact. Mechanical Systems and Signal Processing **125**, 65–78 (2019) https://doi.org/10.1016/j.ymssp.2018.08.011

[6] Ehehalt, U., Alber, O., Markert, R., Wegener, G.: Experimental observations



(a) Disc orbit

(b) Outer-ring trajectory

(c) Time-domain vertical displacement of the disk

(d) Full spectrum of the disk

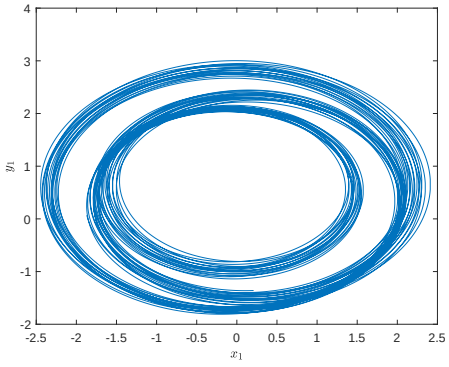
Fig. 22: Responses at $\omega = 1.53$ rad/s under high eccentricity ($e = 1.0$)

on rotor-to-stator contact. Journal of Sound and Vibration **446**, 453–467 (2019) https://doi.org/10.1016/j.jsv.2019.01.048

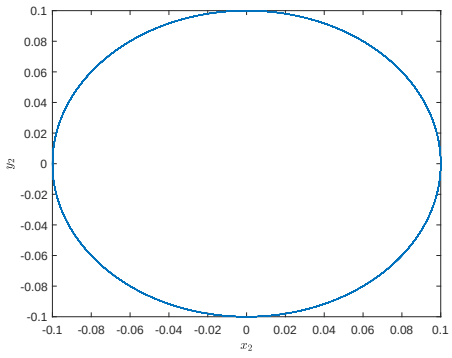
[7] Li, Q., Hu, H., Liao, M., Jing, X.: Insight on uncertainty of geometrically nonlinear rotor with rub-impact under maneuvering motion. Mechanical Systems and Signal Processing (2023) https://doi.org/10.1016/j.ymssp.2023.110334

[8] Ehrich, F.F.: High order subharmonic response of high speed rotors in bearing clearance. ASME Journal of Vibration, Acoustics, Stress, and Reliability in Design **110**(1), 9–15 (1988) https://doi.org/10.1115/1.3269438

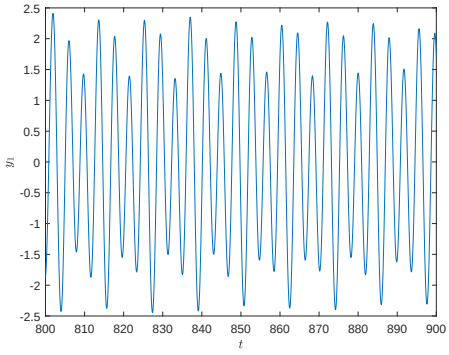
[9] Childs, D.W.: Fractional-frequency rotor motion due to nonsymmetric clearance effects. ASME Journal of Engineering for Power **104**, 533–541 (1982) https://doi.org/10.1115/1.3227316



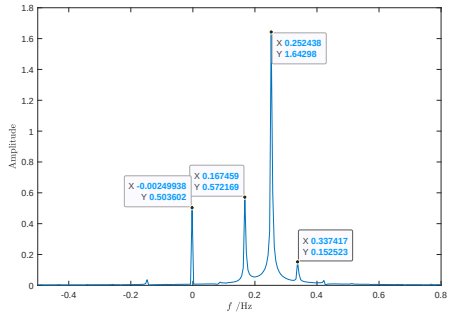
(a) Disc orbit



(b) Outer-ring trajectory



(c) Time-domain vertical displacement of the disk



(d) Full spectrum of the disk

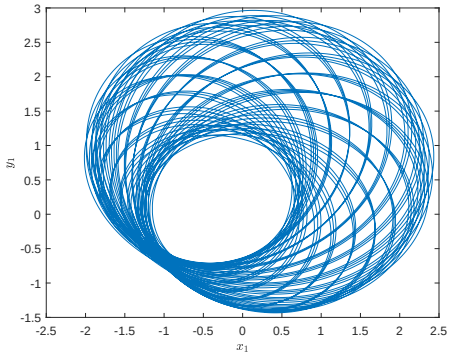
Fig. 23: Responses at $\omega = 1.61$ rad/s under high eccentricity ($e = 1.0$)

[10] Choi, Y.S., Noah, S.T.: Nonlinear steady-state response of a rotor-support system. ASME Journal of Vibration, Acoustics, Stress, and Reliability in Design **109**(3), 255–261 (1987) https://doi.org/10.1115/1.3269428

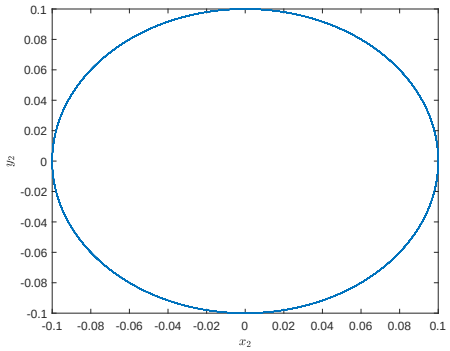
[11] Kim, Y.B., Noah, S.T.: Bifurcation analysis for a modified jeffcott rotor with bearing clearance. Nonlinear Dynamics **1**, 221–241 (1990) https://doi.org/10.1007/BF01858275

[12] Tiwari, M., Gupta, K., Prakash, O.: Effect of radial internal clearance of a ball bearing on the dynamics of a balanced horizontal rotor. Journal of Sound and Vibration **238**(5), 723–756 (2000) https://doi.org/10.1006/jsvi.2000.3145

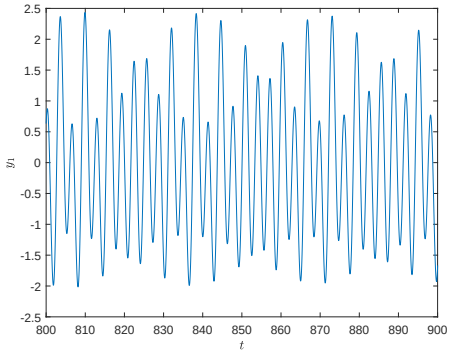
[13] Tiwari, M., Gupta, K., Prakash, O.: Dynamic response of an unbalanced rotor supported on ball bearings. Journal of Sound and Vibration **238**(5), 757–779 (2000) https://doi.org/10.1006/jsvi.2000.3144



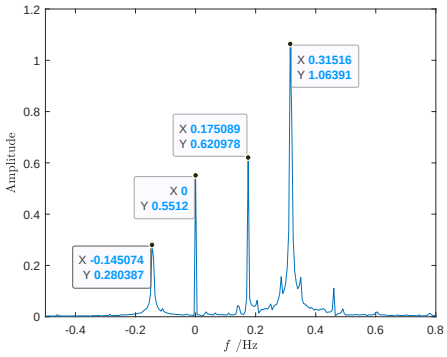
(a) Disc orbit



(b) Outer-ring trajectory



(c) Time-domain vertical displacement of the disk



(d) Full spectrum of the disk

Fig. 24: Responses at $\omega = 1.99$ rad/s under high eccentricity ($e = 1.0$)

[14] Harsha, S.P.: Nonlinear dynamic response of a balanced rotor supported by rolling element bearings due to radial internal clearance effect. Mechanism and Machine Theory **41**(6), 688–706 (2006) https://doi.org/10.1016/j.mechmachtheory.2005.08.003

[15] Cao, H., Shi, F., Li, Y., Li, B., Chen, X.: Vibration and stability analysis of rotor-bearing-pedestal system due to clearance fit. Mechanical Systems and Signal Processing **133** (2019) https://doi.org/10.1016/j.ymssp.2019.106275

[16] Xu, H., Wang, P., Ma, H., Yang, Y., Li, X., Luo, Z., Wen, B.: Dynamic behaviors and contact characteristics of ball bearings in a multi-supported rotor system under the effects of 3d clearance fit. Mechanical Systems and Signal Processing **196** (2023) https://doi.org/10.1016/j.ymssp.2023.110334

[17] Wang, S.J., Liao, M.F., Liu, Y.Q., Wang, D.Y., Jiang, Y.F., Liao, J., Li, H.: Nonlinear vibration of rotor systems caused by assembly process of a bearing

outer ring of an aero-engine. Journal of Aerospace Power **30**(1), 82–89 (2015) https://doi.org/10.13224/j.cnki.jasp.2015.01.012

[18] Wu, D., Han, Q., Wang, H., Zhou, Y., Wei, W., Wang, H., Xie, T.: Nonlinear dynamic analysis of rotor-bearing-pedestal systems with multiple fit clearances. IEEE Access **8**, 26715–26725 (2020) https://doi.org/10.1109/ACCESS.2020.2971326

[19] Han, Q., Qin, Z., Chu, F.: Nonlinear dynamic analysis of flywheel rotor systems with multiple fit clearances. In: Advances in Applied Nonlinear Dynamics, Vibration and Control (2024). Conference paper

[20] Zhang, K., Wang, Z., Gao, L., *et al.*: Research for the bearing fit effect on the vibration characteristics of spindle rotor-bearing system. Journal of Mechanical Science and Technology **37**(12), 6257–6270 (2023) https://doi.org/10.1007/s12206-023-1104-3

[21] Wang, H., Chen, G., Song, D.: Passive vibration reduction of a squeeze film damper for a rotor system with fit looseness between outer ring and housing. Proceedings of the Institution of Mechanical Engineers, Part C: Journal of Mechanical Engineering Science (2021) https://doi.org/10.1177/0954406220969625

[22] Lu, H., Li, W., Shen, J., Chen, T., Sheng, L.: Dynamic characteristics analysis of rotor-bearing system considering bearing clearance and hybrid eccentricity. Journal of Vibration Engineering & Technologies **12**, 2249–2263 (2024) https://doi.org/10.1007/s42417-023-00977-7

[23] Yamamoto, T., Ishida, Y.: Linear and Nonlinear Rotordynamics: A Modern Treatment with Applications. John Wiley & Sons, New York (2001)

[24] Zhao, L., Zhai, R., Yan, Z., *et al.*: Nonlinear vibration mechanism of elastic beam in large overall rotation with rotor eccentricity effect. Machine Tool & Hydraulics **52**(7), 6–14 (2024)

[25] Liu, J., Zhang, L., Yin, F., *et al.*: Analysis of the nonlinear response of the friction rotor-oil film bearing system. Journal of Mechanical Strength **42**(6), 1310–1315 (2020)

[26] Zhou, S., Guo, W., Xiao, Q., Zhu, J., Zhou, X., Tu, W.: Vibration characteristics analysis of emu traction motor rotor under eccentric faults. Engineering Mechanics **38**(7), 216–225 (2021)

[27] Zhang, L.-y., Zheng, Y.-q., Cao, Y.-y.: Research on global dynamics of rotor systems considering geometric eccentricity and rub-impact. Nonlinear Dynamics **114**(9) (2026) https://doi.org/10.1007/s11071-026-12558-w

Declarations

Funding

This work was supported by the National Natural Science Foundation of China (Grant Nos. 52105105 and 52272436), the Industry-University-Research Cooperation Project of Aero Engine Corporation of China (Grant No. HFZL2022CXY021), the Application and Innovation Project of Aero Engine Corporation of China (Grant No. 630010504), the Key Project of the Civil Aviation Joint Fund of China (Grant No. U2233204), the Open Fund of the State Key Laboratory of Mechanical Transmission for Advanced Equipment (Grant No. SKLMT-MSKFKT-202301), and the Experimental Technology Research and Development Project of Nanjing University of Aeronautics and Astronautics (Grant No. SYJS202609Z).

Competing Interests

The authors have no relevant financial or non-financial interests to disclose.

Author Contributions

Haifei Wang established the theoretical model and performed the numerical simulations and data processing. Kelong Guo wrote the original manuscript and prepared the figures. Xunkai Liang, Tian Zhou, Chao Dong, Zhenhuan Tang, and Kian Meng Lim contributed to the methodology development, model refinement, and interpretation of the results. All authors reviewed and approved the final manuscript.

Data Availability

The datasets generated during and/or analysed during the current study are available from the corresponding author on reasonable request.